SusMat

WILEY

SusMat

RESEARCH ARTICLE OPEN ACCESS

Hydrogen Storage of Mg Under an Ultralow Pressure of 1 Bar

Xuechun Hu | Yuchen Pang | Chaoqun Li | Xiaoyue Zhang | Xuebin Yu | Fang Fang | Guanglin Xia

College of Smart Materials and Future Energy, Fudan University, Shanghai, China

Correspondence: Fang Fang (f_fang@fudan.edu.cn) | Guanglin Xia (xiaguanglin@fudan.edu.cn)

Received: 30 July 2025 | **Revised:** 26 August 2025 | **Accepted:** 23 September 2025

Keywords: catalyst | hydrogen storage material | magnesium | magnesium hydride | transition metal oxide

ABSTRACT

Magnesium hydride (MgH_2) has been regarded as an attractive candidate for solid-state hydrogen storage, yet its practical applications are limited by the requirement of elevated temperatures and sluggish hydrogen uptake and release kinetics. Herein, TiO_2 polyhedral frameworks with uniformly distributed V_2O_5 (denoted as V_2O_5/TiO_2) are constructed to improve hydrogen storage performance of Mg/MgH_2. During the reversible hydrogenation and dehydrogenation process, metallic V and Ti along with low-valent Ti- and V-based oxides are in situ formed. Among them, metallic V supported on TiO_2 exhibits the lowest hydrogen adsorption energy, enabling superior catalytic performance over TiO_2 and V_2O_5. As a result, the peak dehydrogenation temperature of MgH_2 decreases to 215°C, 105°C lower than that of pristine MgH_2, with a decrease of the apparent activation energy from 139.50 kJ·mol^{-1} to 68.99 kJ·mol^{-1}. Moreover, electron migration from V toward TiO_2 leads to charge accumulation around Ti and O atoms, shifting the V 3*d*-band center toward the Fermi level and thereby improving the catalytic function of V's d-electrons, facilitating hydrogen dissociation without energy barriers. Therefore, the V_2O_5/TiO_2-catalyzed Mg absorbs 4.12 wt% H_2 under an ultralow pressure of 1 bar at 25°C. This provides a new strategy for developing advanced Ti and V-based catalysts for mild-condition hydrogen storage of MgH_2.

1 | Introduction

The growing global environmental issues urgently call for the creation of efficient and sustainable clean energy alternatives to mitigate the ongoing energy crisis. Owing to its outstanding energy density, carbon-free combustion nature, and widespread availability, hydrogen is regarded as a key energy vector for future sustainable systems [1–5]. Nevertheless, the extensive adoption of hydrogen-related technologies is still hindered by insufficient storage and transport approaches. Solid-state hydrogen storage materials distinguish themselves from other storage approaches through their high volumetric density and enhanced safety characteristics, offering a safer and more compact alternative to conventional methods [6–11]. Among them, MgH_2 exhibits an excellent theoretical gravimetric hydrogen capacity of 7.6 wt%, along with remarkable thermal stability and reversibility [12–14]. The hydrogen absorption and desorption mechanism are based on a reversible phase transformation ($Mg + H_2 \leftrightarrow MgH_2$), facilitating secure and controllable reversible hydrogen storage. Furthermore, the abundance of magnesium ranked as the eighth most common element in the Earth's crust ensures widespread availability and economic viability, enhancing the commercial potential of Mg-based hydrogen storage systems [15–18]. Despite these advantages, MgH_2 still encounters critical challenges, such as substantial thermodynamic stability ($\Delta H = -74$ kJ·mol^{-1}) and sluggish kinetics ($E_a = 160$ kJ·mol^{-1}), which results in hydrogen desorption temperatures typically exceeding 300°C. Additionally, its reversible hydrogenation process demands harsh conditions (>30 bar H_2 pressure, >300°C), thereby imposing significant constraints on practical utilization [19, 20]. Developing hydrogen

X. Hu and Y. Pang contributed equally to this work.

storage materials with functionality in low-temperature and low-pressure conditions could enable their use in applications demanding higher safety and portability, like residential energy storage in cold climates and high-precision aerospace systems.

Extensive research has been devoted to enhancing hydrogen storage properties through nanoscale engineering, catalytic modification, or combinatorial approaches [21–23]. Transition metal-based catalysts have been extensively validated for their effectiveness in reducing the energy barriers associated with hydrogen absorption and desorption processes in MgH_2. Among various catalytic materials, titanium-based oxides, particularly TiO_2, have attracted considerable attention due to their facile synthesis protocols, morphological tunability, and remarkable catalytic performance [24, 25]. Zhang et al. reported that TiO_2 nanosheets with preferentially exposed (001) facets reduced the dehydrogenation temperature to 260°C, enabling rapid hydrogen release of 6.0 wt% within 3.2 min and efficient hydrogen absorption of 5.8 wt% within 6 min at 240°C [26]. Recent studies have demonstrated that bimetallic and multi-component catalysts often outperform their monometallic counterparts [27]. Bimetallic oxide catalysts leverage synergistic interactions between distinct metal centers to provide enhanced active site density and more favorable electronic structures, thereby significantly amplifying catalytic efficiency. For instance, Meng et al. elucidated that Nb/V interfaces facilitate enhanced electron transfer dynamics, wherein Nb weakens the Mg-H bond while V mitigates excessive hydrogen adsorption on Nb sites [28]. This cooperative effect enabled MgH_2 to desorb 6.0 wt% of hydrogen in just 5 min at 260°C, while $V_4Nb_{18}O_{55}$-catalyzed Mg exhibited complete hydrogenation even at ambient temperature. Zhang et al. Developed a Ti-V-O composite derived from Mxene templates, where the formation of $TiVO_{3.5}$ with a mixed-valence oxide lattice effectively lowered the initial dehydrogenation temperature by 76°C and allowed 5.0 wt% hydrogen desorbed within 10 min at 250°C [29]. The enhanced performance was attributed to the in situ reduction of $TiVO_{3.5}$ to nanoscale Ti and V particles, significantly improving hydrogen desorption kinetics. Although significant progress has been achieved, practical implementation of Ti- and V-based catalysts remains constrained by their high operating thresholds (>260°C) [30–33]. Furthermore, the atomic-level mechanisms governing the synergistic effect of Ti- and V-based catalysts have yet to be fully elucidated, posing challenges for rational catalyst optimization.

In this work, to investigate the synergistic effect of Ti- and V-based species, anatase TiO_2 polyhedral frameworks with uniformly distributed V_2O_5 (denoted as V_2O_5/TiO_2) are synthesized using Ti-based MOFs (MIL-125) as precursors. Compared to pure MgH_2, a remarkable reduction in peak dehydrogenation temperature from 320°C to 215°C (a decrease of 105°C) with a 50% decrease in apparent activation energy is observed under the catalysis of V_2O_5/TiO_2. It is experimentally demonstrated that metallic V and Ti along with other low-valent Ti- and V-based oxides are in situ formed throughout the cycling. Among them, metallic V under the support of TiO_2 exhibits the lowest hydrogen adsorption energy, which enables its superior catalytic performance than pure TiO_2 and V_2O_5. More importantly, the electron transfer from V to the TiO_2 surface leads to the accumulation of electron around Ti and O atoms and hence the spin-up and spin-down *d*-band centers of V 3*d* orbitals shift closer to the Fermi level, which effectively promotes the catalytic capability of *d* electron of V and results in barrierless H_2 dissociation catalyzed by metallic V under the support of TiO_2. As a result, the V_2O_5/TiO_2-catalyzed Mg demonstrates a hydrogen uptake of 4.12 wt% under mild conditions in just 30 min (1 bar H_2 at 25°C).

2 | Results and Discussion

The synthesis procedure of MIL-125 is displayed in Figure 1A. Initially, MIL-125 was prepared via a solvothermal route, after which vanadium species were introduced into the MIL-125 framework using NH_4VO_3 as the vanadium precursor through a post-impregnation process. The resulting brown powder was subsequently calcined, yielding the V_2O_5/TiO_2 composite, hereafter referred to as 0.2VTiO. X-ray diffraction (XRD) patterns confirmed that the as-prepared sample retained the crystal structure of MIL-125, whereas the calcined products exhibited diffraction peaks that match the standard reference cards of anatase TiO_2 (PDF#21-1272) and V_2O_5 (PDF#41-1426), as presented in Figure 1B. The V/Ti molar ratio determined by ICP analysis in the catalyst corresponds precisely to the precursor feed ratio of ammonium metavanadate and Ti-MOF, evidencing full retention of V_2O_5 during incorporation into Ti-MOF (Table S1). The X-ray photoelectron spectroscopy (XPS) spectra revealed distinct V 2p and Ti 2p doublet peaks centered at 516.3/523.6 eV and 458.0/463.7 eV, respectively, consistent with the oxidation states of V^{5+} and Ti^{4+}, confirming the coexistence of V_2O_5 and TiO_2 (Figure 1C). Furthermore, elemental analysis (Figure S1) and XPS survey spectrum (Figure S2) verified the absence of any residual elements in the as-synthesized 0.2VTiO.

The MIL-125 precursor obtained from the solvothermal reaction exhibited well-defined polyhedral structures with varying particle sizes (Figure S3). After thermal calcination, MIL-125 transformed into anatase TiO_2 with V_2O_5 deposited on both internal and external surfaces (Figure 1D,E). Notably, as-synthesized 0.2VTiO retained the polyhedral morphology of MIL-125. This structural preservation could be attributed to the formation of anatase TiO_2 during calcination, which facilitates the uniform dispersion and growth of V_2O_5 on its surface while maintaining the structural integrity of the polyhedral architecture. TEM images revealed that each polyhedron is consisted of nanoparticles with approximately tens of nanometers (Figure S4). HRTEM images revealed distinct lattice fringes with interplanar distances of 0.219 and 0.353 nm, assignable to the (002) planes of V_2O_5 and the (101) planes of anatase TiO_2 (Figure 1F), respectively, in strong accordance with the XRD and XPS characterizations.

Elemental mapping based on EDS further demonstrated the homogeneous distribution of V, Ti, and O throughout the 0.2VTiO (Figure 1G). For comparative purposes, bulk V_2O_5, TiO_2, and physical mixed V_2O_5/TiO_2 (denoted as m-VTiO) were also synthesized following similar procedures, resulting in particles with micrometer dimensions and irregular morphologies, as evidenced by SEM images in Figure S5.

The introduction of 0.2VTiO with different doping mass ratios into MgH_2 was realized by ball-milling. After that, XRD analysis revealed weak characteristic diffraction peaks of MgH_2 under 0.2VTiO catalysis, while 0.2VTiO peaks were absent (Figure S6),

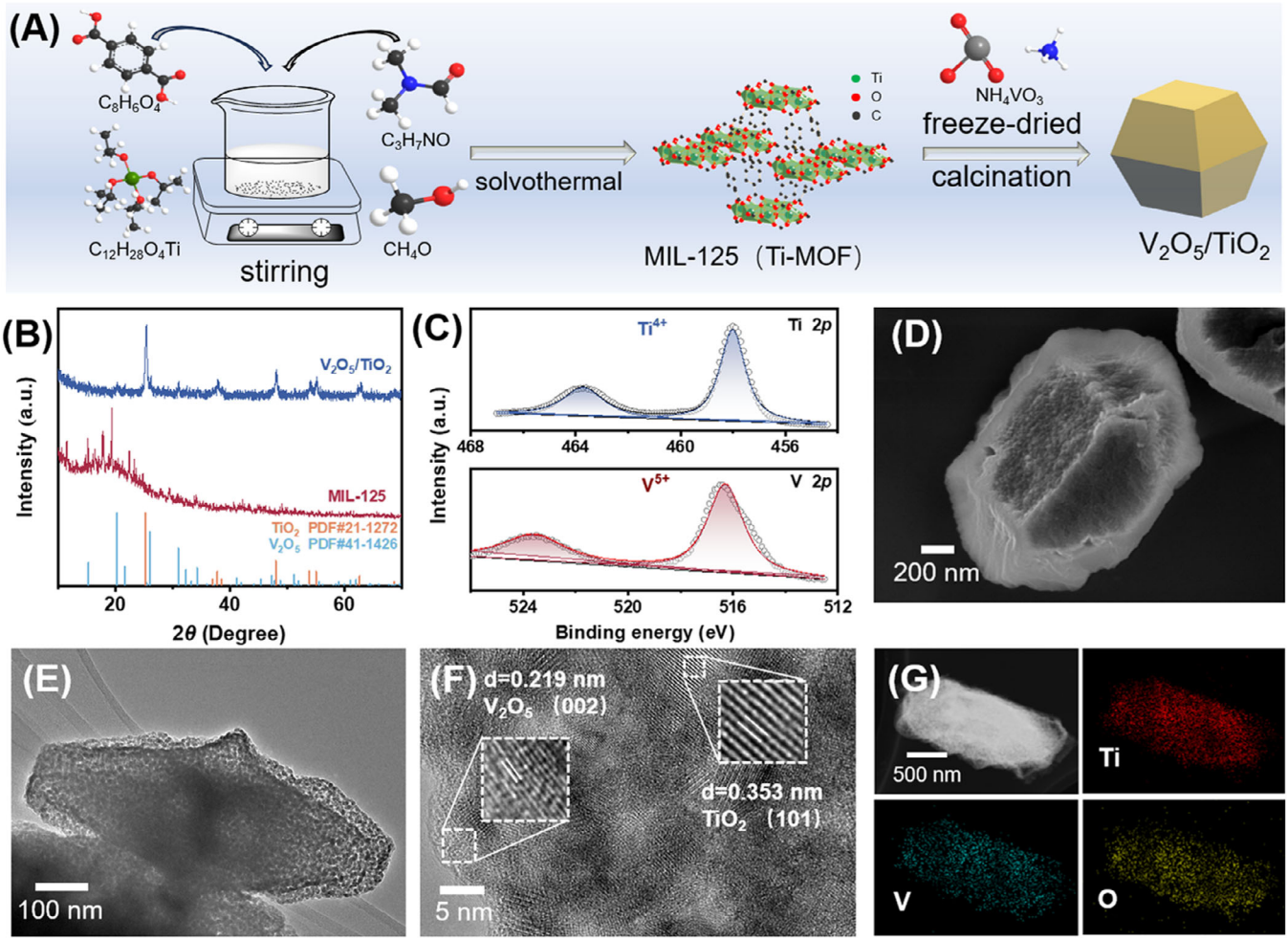

FIGURE 1 | (A) The preparation process of V_2O_5/TiO_2 bimetallic oxide. (B) XRD patterns of MIL-125 and V_2O_5/TiO_2 heterostructure. (C) High-resolution Ti 2*p* and V 2*p* XPS spectra of V_2O_5/TiO_2. (D–G) SEM, TEM, HRTEM, STEM and the relative EDS elemental mapping images of V_2O_5/TiO_2.

which may be attributed to its low doping concentration. SEM images indicated that MgH_2 particles after ball milling exhibited dimensions ranging from several to tens of micrometers (Figure S7), whereas the particle size was reduced to approximately 100-800 nm after the introduction of 0.2VTiO. EDS mapping results demonstrated the homogeneous distribution of both V and Ti elements within MgH_2 (Figure S8).

As the vanadium content increases, the onset dehydrogenation temperature initially decreases and subsequently rises, reaching the lowest value (207°C) at a V/Ti molar ratio of 0.2 (Figure S9). SEM images reveal that V_2O_5 preferentially deposits on the inner surface of the TiO_2 framework, where it acts synergistically through the interface (Figure S10). However, the Brunauer–Emmett–Teller (BET) analysis indicates that excessive vanadium loading leads to pore blockage within the MOF framework channels, resulting in a reduced specific surface area from 180.4 $m^2 \cdot g^{-1}$ for 0.2VTiO to 137.4 $m^2 \cdot g^{-1}$ for 0.4VTiO (Figure S11). This results in a reduction of catalytic active sites, and the changes in BET surface area correlate with the variation in the initial dehydrogenation temperature. Based on comprehensive evaluation, 0.2VTiO was selected for subsequent investigations. 0.2VTiO and MgH_2 were then ball-milled at various doping mass ratios, and their hydrogen desorption performances were preliminarily evaluated (Figure 2A). The ball-milled MgH_2 without catalyst exhibited negligible hydrogen release below 300°C, while complete desorption occurred near 400°C, yielding a total hydrogen capacity of 7.53 wt%. In contrast, the inclusion of only 1 wt% 0.2VTiO dramatically reduced the desorption onset by approximately 63°C and enabled over 6.5 wt% hydrogen release below 300°C, highlighting the pronounced catalytic effect of the composite on MgH_2 dehydrogenation. Further reduction in hydrogen desorption temperature was observed with increasing catalyst doping ratio. Considering both the hydrogen desorption rate and capacity, MgH_2 doped with 10 wt% 0.2VTiO was selected for detailed investigation (denoted as MgH_2-0.2VTiO).

As illustrated in Figure 2B, the addition of TiO_2 and V_2O_5 effectively reduced the peak desorption temperatures to 251°C and 237°C, respectively. This observation reveals the strong catalytic contribution of these oxides toward facilitating the hydrogen release process from MgH_2. Upon further introduction of 0.2VTiO, the desorption onset temperature dropped notably to 207°C, while the peak temperature decreased to 225°C, much lower than that of MgH_2 catalyzed by TiO_2 and V_2O_5. These results highlight the synergistic role of TiO_2 and V_2O_5 in promoting hydrogen desorption performance of MgH_2. However, only a peak temperature of approximately 243°C could be observed for

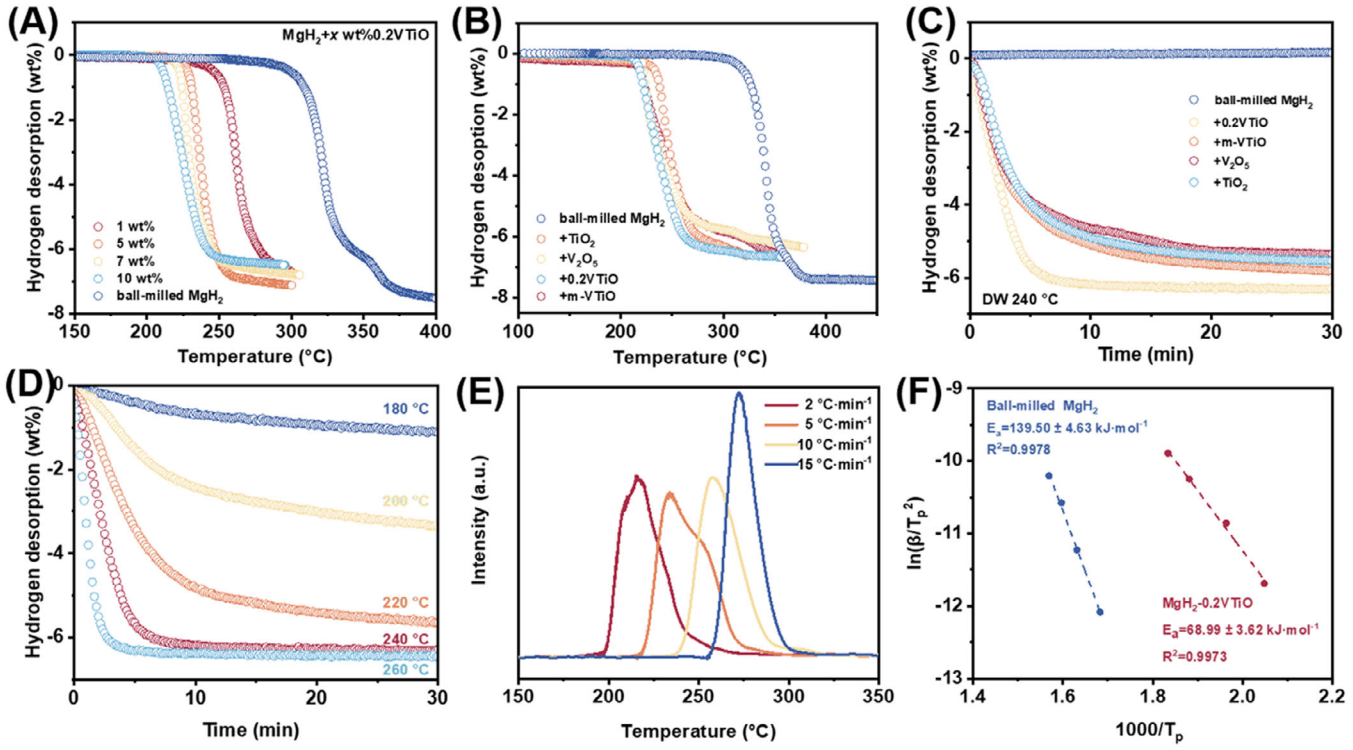

FIGURE 2 | (A) TPD curves of MgH_2-0.2VTiO with various loading ratios. (B) TPD curves of MgH_2 ball-milled with different catalysts. (C) Dehydrogenation performance of MgH_2 with different catalysts at 240°C. (D) Isothermal dehydrogenation curves of MgH_2 catalyzed by 0.2VTiO at different temperatures. (E) The differential curves of the hydrogen desorption of MgH_2 under the catalysis of 0.2VTiO. (F) Fitting results of the apparent activation energy of MgH_2 with and without 0.2VTiO.

MgH_2 catalyzed by m-VTiO, which demonstrates that the uniform distribution of 0.2VTiO achieved during ball milling effectively enhances catalytic efficiency.

Isothermal dehydrogenation tests were conducted at 240°C to compare the kinetic performance of MgH_2 with and without the catalysis of 0.2VTiO (Figure 2C). Notably, ball-milled MgH_2 exhibited negligible hydrogen release at 240°C, whereas MgH_2 under the catalysis of V_2O_5 or TiO_2 released approximately 5 wt% hydrogen within 30 min. Interestingly, after the introduction of m-VTiO, the hydrogen release capacity of MgH_2 could be increased to 5.5 wt%, which provides additional evidence to the synergistic effect between these two metal oxide components. In contrast, MgH_2 catalyzed by 0.2VTiO achieved complete hydrogen desorption within just 10 min, releasing 6.1 wt% hydrogen, demonstrating the superior performance in terms of both desorption rate and capacity compared to all other samples. Isothermal hydrogen desorption at various temperatures illustrated that MgH_2-0.2VTiO achieved almost complete hydrogen desorption within 5 min at 260°C (Figure 2D). At a reduced temperature of 240°C, MgH_2-0.2VTiO was still able to desorb about 6.1 wt% of hydrogen in approximately 10 min, while the hydrogen desorption capacity remained above 5.5 wt% after 30 min of isothermal treatment at 220°C. Even under 180°C, approximately 1 wt% hydrogen could be detected over 30 min.

To quantitatively assess the influence of 0.2VTiO on enhancing the hydrogen desorption kinetics of MgH_2, TPD measurements were conducted on both MgH_2 with and without 0.2VTiO at different heating rates (Figure S12). The hydrogen desorption curves were differentiated to determine the peak desorption temperatures (Figure 2E). At a ramping rate of 2°C·min^{-1}, the peak temperature of MgH_2 catalyzed by 0.2VTiO was reduced from 320°C to 215°C, representing a substantial decrease of 105°C. Subsequently, the hydrogen desorption activation energy (E_a) was calculated using the Kissinger equation to analyze the linear relationship between desorption peak temperatures and heating rates, according to the following equation:

$$\frac{d(\ln\beta/T_p^2)}{d(1/T_p)} = \frac{-E_a}{R}, \quad (1)$$

where β represents the heating rate, T_p denotes the peak temperature, R is the universal gas constant. The activation energy (E_a) is obtained from the slope of the fitted line presented in Figure 2F. The calculated activation energy for ball-milled MgH_2 was 139.50 ± 4.63 kJ·mol^{-1}, while the addition of 0.2VTiO as a catalyst significantly reduced this value to 68.99 ± 3.62 kJ·mol^{-1}, representing approximately a 50% decrease compared to pure MgH_2. This remarkable decrease in energy barrier highlights the strong synergistic catalytic action of 0.2VTiO in facilitating dehydrogenation of MgH_2.

The reversible hydrogen absorption experiments conducted at 50°C under 50 bar revealed that pure Mg exhibited negligible hydrogen absorption capacity. In strong contrast, Mg catalyzed by V_2O_5 and TiO_2 absorbed 4.12 wt% H_2 and 4.31 wt% H_2 after 30 min, while that of 0.2VTiO-catalyzed Mg reached 5.15 wt% H_2, demonstrating the superior catalytic effect of 0.2VTiO in improving Mg hydrogenation than both V_2O_5 and TiO_2 (Figure S13).

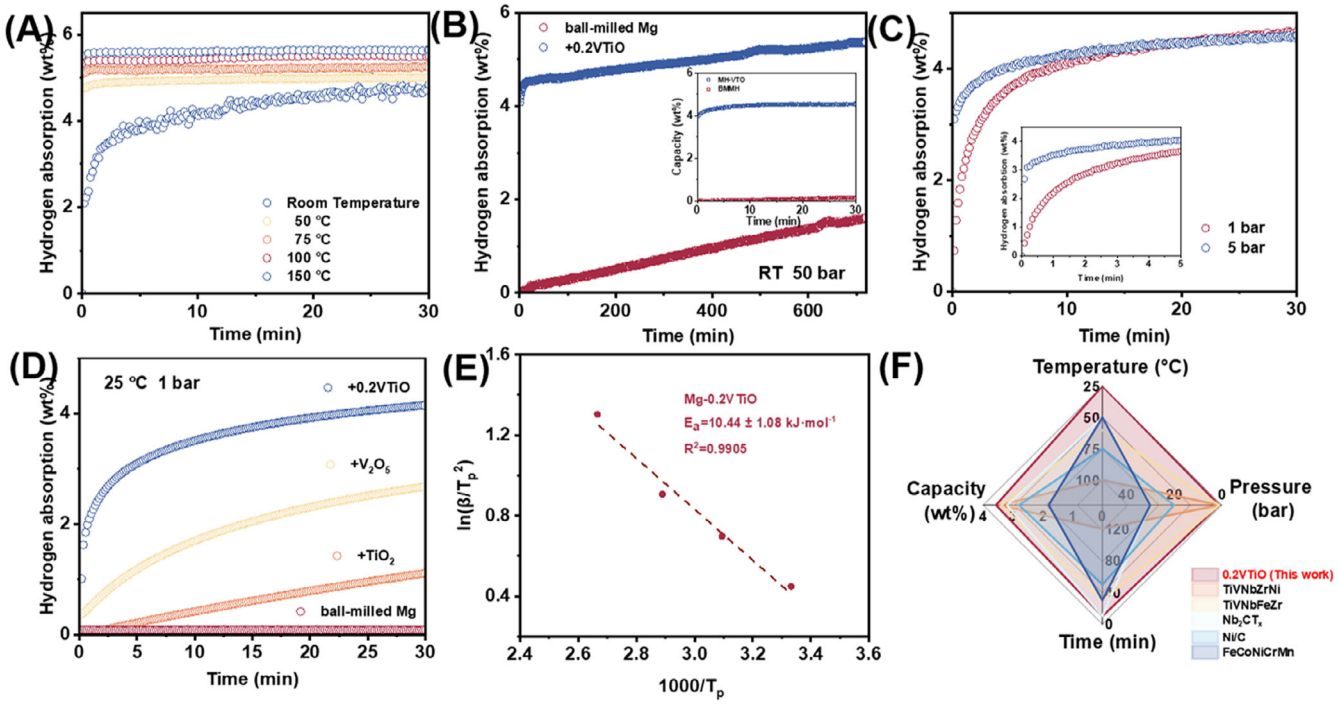

FIGURE 3 | Hydrogen absorption curves of (A) Mg catalyzed by 0.2VTiO at 50 bar H_2 and different temperatures, (B) Mg with and without the catalysis of 0.2VTiO at room temperature and 50 bar H_2, (C) Mg catalyzed by 0.2VTiO under 1 and 5 bar H_2 conditions, and (D) Mg catalyzed by 0.2VTiO, V_2O_5, TiO_2, and Mg under conditions of 25°C and 1 bar H_2. (E) The activation energy of Mg catalyzed by 0.2VTiO. (F) Radar chart comparing the hydrogen storage performance of Mg catalyzed by different catalysts based on temperature, pressure, time, and hydrogen absorption capacity [34–38].

Remarkably, under the catalysis of 0.2VTiO, Mg absorbed 4.6 wt% hydrogen within 30 min even at room temperature (Figure 3A).

A comparative assessment of hydrogen absorption performance between ball-milled Mg and 0.2VTiO-catalyzed counterpart at room temperature (Figure 3B) revealed a distinct difference. The untreated Mg gradually absorbed only 1.57 wt% hydrogen over 12 h, whereas 0.2VTiO-catalyzed Mg rapidly absorbed more than 4 wt% hydrogen during the initial stage and achieved a total absorption capacity of 5.33 wt% with extended exposure time. Significantly, 0.2VTiO-catalyzed Mg maintained hydrogen absorption efficiency even under an ultralow hydrogen pressure of 1 bar (Figure 3C). At 50°C under hydrogen pressures of 1 and 5 bar, the composite absorbed 4.11 wt% and 4.23 wt% hydrogen within 10 min, respectively, further substantiating the enhanced hydrogenation performance facilitated by 0.2VTiO. While pure Mg exhibited no detectable hydrogen absorption under these conditions, Mg catalyzed by V_2O_5 and TiO_2 gradually absorbed 2.51 wt% and 1.11 wt% hydrogen over 30 min. In contrast, 0.2VTiO-catalyzed Mg rapidly absorbed 3.10 wt% hydrogen within just 5 min and achieved a total absorption capacity of 4.12 wt% after 30 min (Figure 3D). Moreover, the activation energy for hydrogen uptake by Mg in the presence of 0.2VTiO catalyst reaches only 10.44 $kJ \cdot mol^{-1}$, representing a marked improvement over pure Mg (Figure 3E). These results confirm that 0.2VTiO functions as an effective catalyst for improving both hydrogen absorption and desorption processes in the Mg/MgH_2 system. The performance of hydrogen absorption is superior to some previously reported results across multiple key indicators (Figures 3F).

Pressure-composition isotherm (PCI) curves of MgH_2 catalyzed by 0.2VTiO at various temperatures indicated that the equilibrium plateau pressures were determined to be 0.24, 0.52, 1.28, and 2.68 bar at 250°C, 275°C, 300°C, and 325°C, respectively (Figure S14A). According to the van't Hoff equation, the thermodynamic enthalpy value (ΔH) of 78.1 ± 2.4 $kJ \cdot mol^{-1}$ was obtained for MgH_2 catalyzed by 0.2VTiO (Figure S14B), which is comparable to the value of 79.7 ± 0.3 $kJ \cdot mol^{-1}$ obtained for ball-milled MgH_2 (Figure S15). This similarity in enthalpy values confirms that adding 0.2VTiO has negligible impact on MgH_2's thermodynamic characteristics. Thus, enhanced hydrogen storage capabilities stem primarily from kinetic improvements induced by the 0.2VTiO catalyst, which accelerates both H_2 uptake and release reactions.

Cycling performance tests were conducted under conditions of hydrogen desorption at 260°C and the rehydrogenation at 250°C under 50 bar H_2 pressure (Figure 4A,B). During the initial dehydrogenation cycle, MgH_2 catalyzed by 0.2VTiO released 6.35 wt% hydrogen. However, the capacity decreased to 6.01 wt% in the second cycle, representing approximately 94.6% of the initial capacity. The reversible capacity was well preserved after the third cycle and reached 5.57 wt% after ten cycles of hydrogen storage process, corresponding to 87.7% of the first-cycle capacity. This initial capacity degradation suggests the formation of irreversible phases involving magnesium. XRD analysis of MgH_2 catalyzed by 0.2VTiO after 10 cycles revealed weak diffraction peaks associated with MgO (PDF#45-0946), which likely accounts for the observed capacity decline (Figure 4C).

To investigate the evolution of Ti and V species during cycling, the high-resolution V 2*p* and Ti 2*p* XPS spectra of

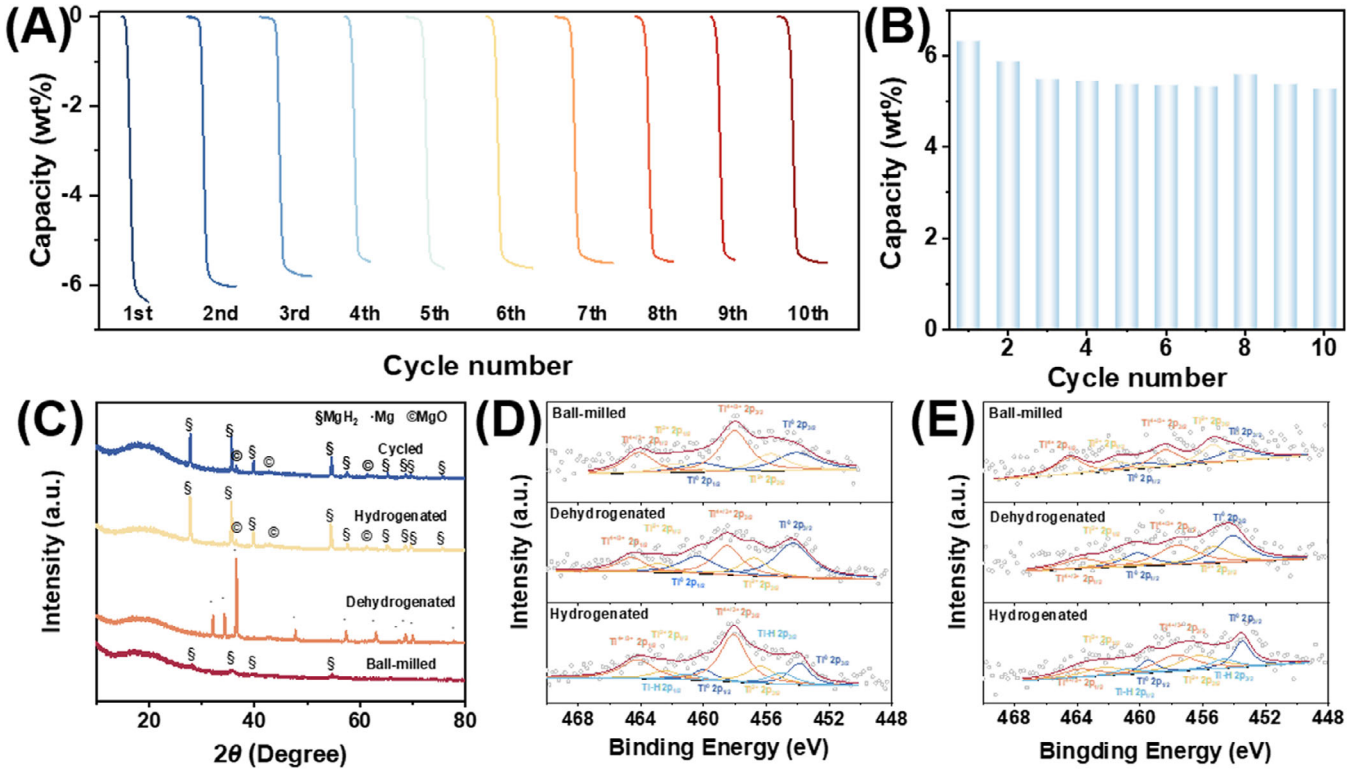

FIGURE 4 | (A) Cyclic hydrogen desorption curve of MgH_2 catalyzed by 0.2VTiO at 260°C. (B) Reversible hydrogen capacity of MgH_2 catalyzed by 0.2VTiO over 10 hydrogen absorption/desorption cycles. (C) XRD patterns of 0.2VTiO-catalyzed MgH_2 at different stages during the reversible process. High-resolution Ti 2*p* XPS spectra of (D) MgH_2 catalyzed by 0.2VTiO and (E) MgH_2 catalyzed by TiO_2 during cycling.

0.2VTiO-catalyzed MgH_2 and TiO_2-catalyzed MgH_2 under cyclic hydrogen absorption/desorption conditions were conducted. The V^{5+} in V_2O_5 undergoes gradual reduction in valence state during cycling, as evidenced by the V 2*p* doublet peaks at 512.2 eV and 519.8 eV, which are indicative of the formation of metallic vanadium (V^0). Notably, the V^{5+} signal becomes nearly undetectable, confirming the reduction of V_2O_5 to lower-valent vanadium species and V^0 (Figure S16). The relative peak areas were employed for semi-quantitative analysis of Ti valence state variations. Notably, in the presence of vanadium, higher-valence Ti species undergo reduction to lower oxidation states during hydrogen desorption, as evidenced by the increased relative peak area of the Ti^0 doublet at 454.1 eV and 460.2 eV (Figure 4D). Compared to TiO_2-catalyzed MgH_2, more Ti^0 is generated in the presence of V (Figure 4E). Conversely, during hydrogen absorption, partial Ti^0 undergoes hydrogenation to form TiH_2, resulting in a decrease of Ti° content. The formed TiH_2 could further utilize the "hydrogen pump" effect to accelerate the dehydrogenation kinetics of MgH_2 [39].

The microstructural evolution of MgH_2-0.2VTiO during repeated hydrogen absorption/desorption cycles was further investigated (Figure 5A–C). HRTEM analysis of the dehydrogenated sample revealed distinct lattice fringes with an interplanar spacing of 0.245 nm, which can be indexed to the (101) plane of metallic Mg (Figure 5D). In contrast, the hydrogenated and cycled samples displayed lattice fringes with an interplanar spacing of 0.252 nm, characteristic of the MgH_2 (101) plane. These observations provide direct evidence for the reversible phase transformation between Mg and MgH_2, corroborating XRD results presented in Figure 4C. After dehydrogenation, HRTEM analysis revealed not only the presence of the original TiO_2 phase but also the formation of metallic titanium, as evidenced by lattice fringes of 0.224 nm indexed to the Ti (101) plane. After rehydrogenation, new fringes of 0.221 nm were observed (Figure 5E), attributable to the (110) plane of titanium hydride (TiH_2). Additionally, the vanadium component underwent transformation from its initial V^{5+} state in V_2O_5 to reduced species, including metallic vanadium and V_2O_3, as evidenced by characteristic lattice spacings of 0.124 nm and 0.318 nm, respectively. These in situ formed multivalent species (Ti, TiH_2, TiO_2, V, V_2O_3) serve as the actual catalytic centers that promotes the hydrogen storage behavior of MgH_2 (Figure 5F). The synergistic interaction among these various active species contributes to the optimized kinetics observed in the 0.2VTiO-catalyzed MgH_2. STEM and EDS elemental mapping performed on the cycled samples revealed that both vanadium and titanium maintained their uniform distribution throughout the MgH_2-0.2VTiO even after 10 hydrogen absorption/desorption cycles (Figure S17).

The catalytic contribution of the 0.2VTiO-derived species to the hydrogen storage behavior of MgH_2 was examined through density functional theory (DFT) analysis. As shown in Figure 6A, the Mg–H bond length in pure MgH_2 is 1.72 Å. Under the influence of TiO_2 and V_2O_3, both O–Mg and Ti–H interactions emerge, elongating the Mg–H bond to 1.94 Å and 2.00 Å. In contrast, the presence of V and Ti leads to direct Mg–H bond cleavage, likely due to its strong H affinity (E_{ads} = –1.02 eV/–1.12 eV). A similar effect is observed for V/TiO_2, where H atoms adjacent to V induce Mg–H bond dissociation (Figure 6B). Notably, V supported on

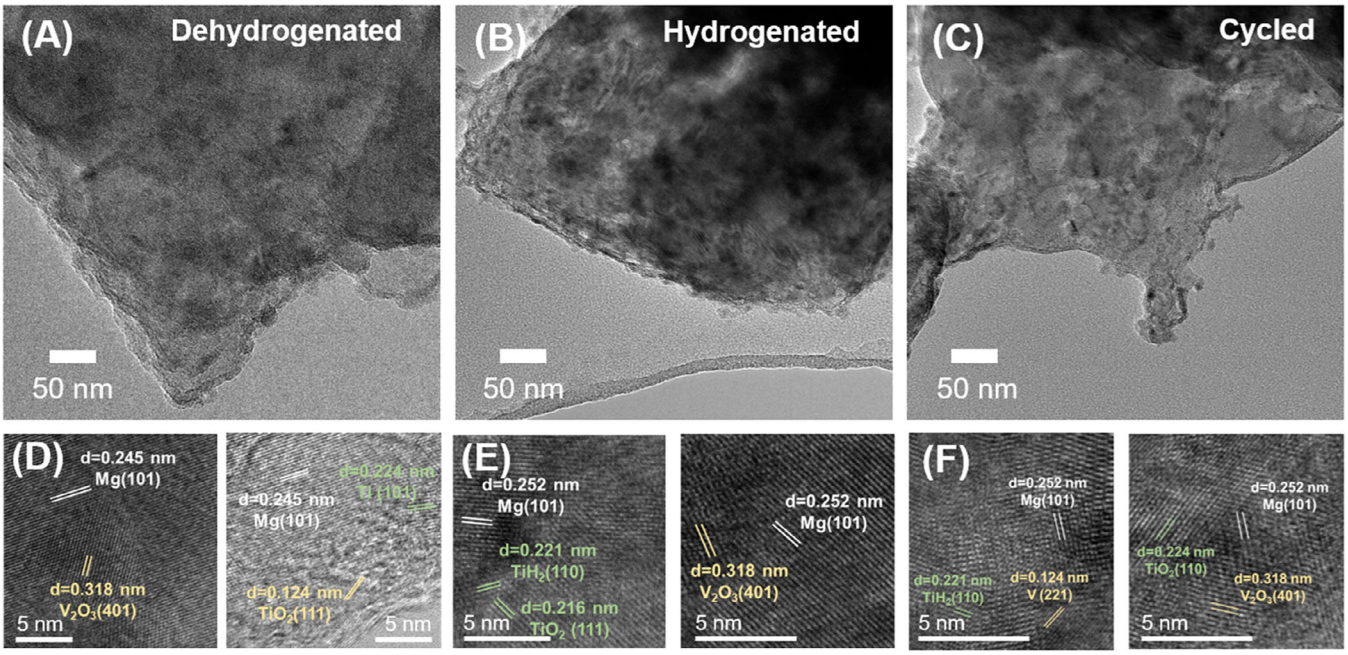

FIGURE 5 | (A–C) TEM and (D–F) the relative HRTEM images of MgH_2 under the catalysis of 0.2VTiO at various states.

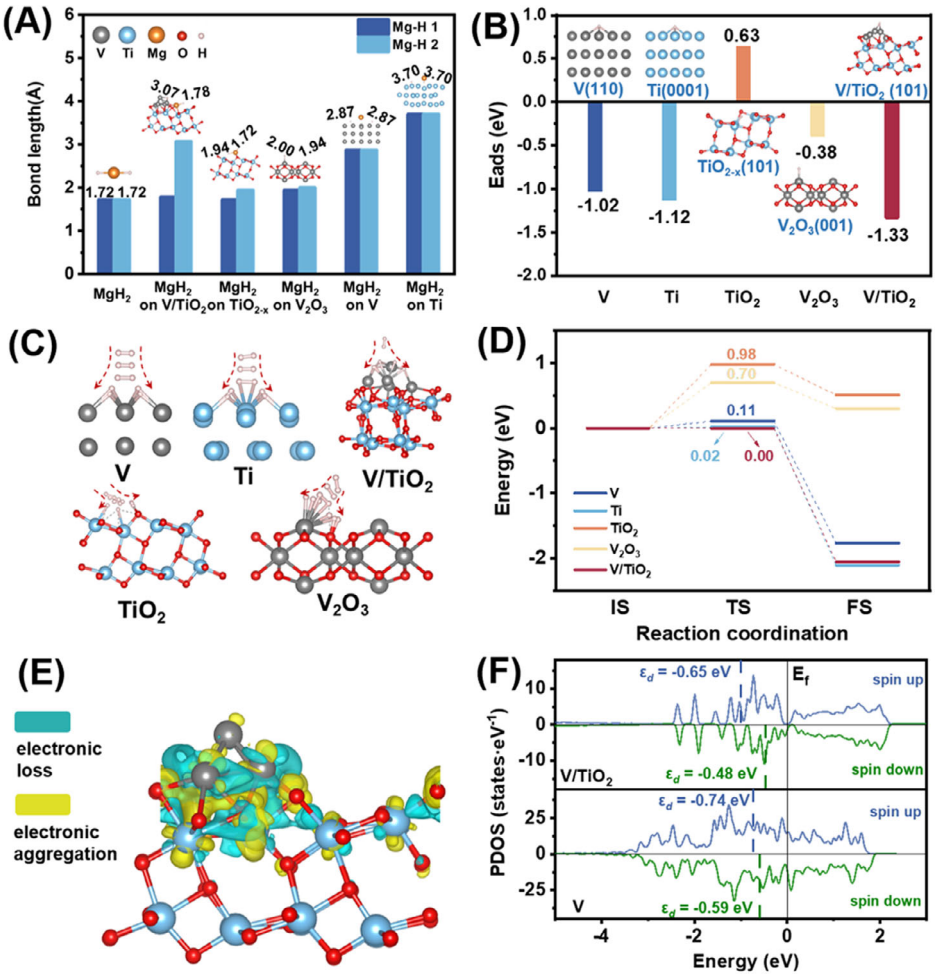

FIGURE 6 | (A) Bond lengths of MgH_2 and MgH_2 doped with V, Ti, V_2O_3, TiO_2, and V/TiO_2. (B) Hydrogen adsorption energy (E_{ads}), (C) H_2 dissociation reaction pathway, and (D) H_2 dissociation energy barrier of V, Ti, V_2O_3, TiO_2, and V/TiO_2. (E) Charge density difference for V/TiO_2 (equivalent surface 0.01 e·Bohr^{-3}, yellow area represents electron aggregation while the blue area represents electron loss). (F) Projected density of states (PDOS) of V 3*d* orbitals in V and V/TiO_2.

TiO_2 exhibits an even lower H adsorption energy (–1.33 eV), indicating a stronger ability to abstract H from MgH_2, which enables superior catalytic performance of 0.2VTiO than TiO_2 and V_2O_5. On the other hand, V/TiO_2 enables barrierless H_2 dissociation, while TiO_2 and V individually exhibit energy barriers of 0.98 eV and 0.11 eV, respectively (Figure 6C,D). This implies that in situ formed V species embedded in TiO_2 during the hydrogen storage of MgH_2 under the catalysis of 0.2 VTiO synergistically enhance H_2 activation and facilitate hydrogen absorption.

Charge density difference mapping shows electron migration from V toward the TiO_2 surface, leading to localized electron enrichment near Ti and O atoms (Figure 6E). Induced by this phenomenon, the spin-up and spin-down *d*-band centers of V 3*d* orbitals shift closer to the Fermi level by 0.09 eV and 0.11 eV, respectively (Figure 6F), in the projected density of states (PDOS) analysis results, which enhances the catalytic capability of *d* electron of V. This leads to much lower energy barriers of hydrogen dissociation and superior hydrogen absorption ability of V supported on TiO_2 than pure V [40]. These findings demonstrate that the V/TiO_2 composite significantly enhances the reversible hydrogen storage performance of MgH_2 through synergistic catalytic effects, exhibiting superior catalytic properties compared to pure TiO_2 or V_2O_5.

3 | Conclusion

In this work, anatase TiO_2 polyhedral framework with uniformly distributed V_2O_5 (denoted as V_2O_5/TiO_2) is synthesized using Ti-based MOFs (MIL-125) as precursors. It is experimentally demonstrated that, throughout the cycling process, metallic V and Ti along with other low-valent Ti- and V-based oxides are in situ formed. Among them, V supported on TiO_2 exhibits a H adsorption energy of –1.33 eV, considerably lower than V and TiO_2, suggesting a pronounced synergistic interaction between V and TiO_2 in facilitating hydrogen desorption/absorption reactions. As a result, in comparison with pure MgH_2, a remarkable reduction in peak desorption temperature from 320°C to 215°C (a decrease of 105°C) with a 50% decrease in apparent activation energy (from 139.50 kJ·mol^{-1} to 68.99 kJ·mol^{-1}) could be observed under the catalysis of V_2O_5/TiO_2. More importantly, the electron transfer from V to the TiO_2 surface leads to the accumulation of electron around Ti and O atoms and hence the spin-up and spin-down *d*-band centers of V 3*d* orbitals shift closer to the Fermi level, which effectively enhances the catalytic capability of *d* electron of V and results in barrierless H_2 dissociation catalyzed by metallic V under the support of TiO_2. Therefore, the V_2O_5/TiO_2-catalyzed Mg delivered a rapid hydrogen uptake of 4.12 wt% at 25°C under 1 bar H_2. By comparison, no detectable hydrogen absorption could be observed under identical conditions. This work provides a new strategy for developing advanced Ti- and V-based catalysts to realize hydrogen storage of MgH_2 under mild conditions.

4 | Experimental Section

4.1 | Reagents

Terephthalic acid (PTA), titanium tetraisopropanolate (TPT), and ammonium metavanadate (NH_4VO_3) were obtained from Aladdin Industrial Corporation. Methanol (CH_3OH) and N,N-Dimethylformamide (DMF) were obtained from Sinopharm Chemical reagent Co., Ltd. Magnesium hydride (MgH_2) was obtained from Sigma-Aldrich. All chemicals were used directly without further purification.

4.2 | Synthesis of xV_2O_5/TiO_2 Bimetallic Oxide

Firstly, 3.53 g PTA was dissolved in a mixture of 6 mL methanol and 54 mL DMF, with continuous stirring for half an hour. Subsequently, 2.1 mL TPT was introduced into the solution and stirred for half an hour again. The resulting mixture was then subjected to solvothermal treatment at 150°C for 16 h. The precipitated product was purified several times with methanol to remove residual DMF. The purified product was vacuum-dried overnight at 80°C to obtain MIL-125.

For the vanadium loading, 30 mg NH_4VO_3 was dissolved in 30 mL deionized water as vanadium source. Then, 500 mg of the as-synthesized MIL-125 was dispersed uniformly in the above solution with stirring at ambient temperature for 3 h. The obtained suspension was freeze-dried at −196.15°C for 48 h and subsequently calcined in air at 400°C for 4 h. The final products were V_2O_5/TiO_2, denoted as 0.2VTiO. By adjusting the mass of NH_4VO_3, V_2O_5/TiO_2 with different vanadium loadings can be obtained, denoted as *x*VTiO (where *x* represents the molar ratio of V to Ti, $x = 0.05, 0.1, 0.4$).

4.3 | Synthesis of MgH_2-V_2O_5/TiO_2 Composite

MgH_2-*y* wt% *x*VTiO composites (where $y = 1, 5, 7, 10$) were synthesized by incorporating varying doping ratio of *x*VTiO into MgH_2 via high-energy ball milling. The milling process was conducted under the milling speed of 500 rpm for 12 h with a hydrogen pressure of 50 bar, which was maintained to avoid the decomposition of MgH_2 resulting from localized high temperatures generated during the mechanical milling process. All above operations were handled in a high-purity argon-filled glove box with H_2O and O_2 below 0.01 ppm to prevent oxidation. For comparison, V_2O_5 obtained by calcination of NH_4VO_3, TiO_2 obtained by calcination of MIL-125, and bimetallic oxide (m-VTiO) obtained by calcining the physical mixture of NH_4VO_3 and MIL-125 were also introduced into MgH_2 according to the above procedure at a fixed ratio of 10 wt%, denoted as MgH_2-V_2O_5, MgH_2-TiO_2, MgH_2-m-VTiO, respectively.

4.4 | Characterization

SEM (JEOL JSM-6701F) and TEM (JEOL JEM-2011F) were employed to characterize the morphology of the obtained materials. EDS was used to determine the elemental composition in combination with TEM observations. XRD (D8 advance, Bruker AXS) was applied to identify the crystalline phases and structural characteristics of the samples, using Cu Kα radiation (50 kV, 30 mA). To prevent oxidation during testing, all samples were sealed with amorphous tape in an argon-filled glove box. XPS (Thermo Scientific K-Alpha+) was employed to analyze the surface chemical states of the elements.

4.5 | Hydrogen Storage Performance Evaluation

All hydrogen absorption/desorption measurements were conducted using the volumetric method on a laboratory-constructed high-pressure gas sorption apparatus (HPSA). TPD tests were carried out by heating approximately 20 mg of sample under an initial pressure of <0.0001 bar until the sample was completely dehydrogenated. Isothermal dehydrogenation tests were evaluated at various constant temperatures (180°C, 200°C, 220°C, 240°C, and 260°C), where samples were rapidly heated to the target temperature followed by isothermal holding. Hydrogenation measurements were conducted using approximately 100 mg of sample under various hydrogen pressures (1, 5, and 50 bar). Pressure-composition isotherms (PCI) curves were obtained by initially applying hydrogen pressure of approximately 10 bar, heating the sample to the designated temperature, and subsequently recording the pressure throughout the absorption/desorption process.

4.6 | Computational Method

The projector augmented wave (PAW) approach, as realized in the Vienna Ab initio Simulation Package (VASP), was employed for the density functional theory (DFT) computations. The generalized gradient approximation (GGA) formulated by Perdew, Burke, and Ernzerhof (PBE) was adopted, as this functional has been reported to yield reliable descriptions of atomic adsorption in previous benchmark studies. Dispersion forces were considered by applying the DFT-D3 correction proposed by Grimme. For the surface models, a plane-wave basis set with an energy cutoff of 500 eV was utilized together with Γ-centered *k*-point grids of equivalent density. Spin polarization was included in all calculations, and electronic smearing was treated using the Gaussian method with a width of 0.05 eV. Structural relaxations were continued until the total energy and residual atomic forces converged to below 0.05 eV·Å^{-1} and 1×10^{-5} eV, respectively.

Acknowledgments

This work was financially supported by the National Key R&D Program of China (No. 2021YFB3802400), the National Natural Science Foundation of China (No. U2130208 and 22279020), and the Science and Technology Commission of Shanghai Municipality (No. 23ZR1406500).

Conflicts of Interest

The authors declare no conflicts of interest.

References

1. J. O. Abe, A. P. I. Popoola, E. Ajenifuja, and O. M. Popoola, "Hydrogen Energy, Economy and Storage: Review and Recommendation," *International Journal of Hydrogen Energy* 44, no. 29 (2019): 15072–15086.

2. A. Züttel, A. Remhof, A. Borgschulte, and O. Friedrichs, "Hydrogen: The Future Energy Carrier," *Philosophical Transactions of the Royal Society A: Mathematical, Physical and Engineering Sciences* 368 (2010): 3329–3342.

3. X. Yu, Z. Tang, D. Sun, L. Ouyang, and M. Zhu, "Recent Advances and Remaining Challenges of Nanostructured Materials for Hydrogen Storage Applications," *Progress in Materials Science* 88 (2017): 1–48.

4. Y. Wang, X. Chen, H. Zhang, G. Xia, D. Sun, and X. Yu, "Heterostructures Built in Metal Hydrides for Advanced Hydrogen Storage Reversibility," *Advanced Materials* 32, no. 31 (2020): 2002647.

5. Y. Liu, K. Zhong, K. Luo, M. Gao, H. Pan, and Q. Wang, "Size-Dependent Kinetic Enhancement in Hydrogen Absorption and Desorption of the Li–Mg–N–H System," *Journal of the American Chemical Society* 131, no. 5 (2009): 1862–1870.

6. M. Yang, R. Hunger, S. Berrettoni, B. Sprecher, and B. Wang, "A Review of Hydrogen Storage and Transport Technologies," *Clean Energy* 7, no. 1 (2023): 190–216.

7. Y. Liu, H. Pan, M. Gao, and Q. Wang, "Advanced Hydrogen Storage Alloys for Ni/MH Rechargeable Batteries," *Journal of Materials Chemistry* 21, no. 13 (2011): 4743–4755.

8. Y. Pang, Y. Liu, M. Gao, et al., "A Mechanical-Force-Driven Physical Vapour Deposition Approach to Fabricating Complex Hydride Nanostructures," *Nature Communications* 5, no. 1 (2014): 3519.

9. X. Zhang, S. Ju, C. Li, et al., "Atomic Reconstruction for Realizing Stable Solar-Driven Reversible Hydrogen Storage of Magnesium Hydride," *Nature Communications* 15, no. 1 (2024): 2815.

10. H. Pan, Y. Liu, M. Gao, Y. Zhu, Y. Lei, and Q. Wang, "An Investigation on the Structural and Electrochemical Properties of $La_{0.7}Mg_{0.3}(Ni_{0.85}Co_{0.15})_x$ (x=3.15–3.80) Hydrogen Storage Electrode Alloys," *Journal of Alloys and Compounds* 351, no. 1-2 (2003): 228–234.

11. X. Zhang, C. Li, J. Ye, et al., "Light-Enabled Reversible Hydrogen Storage of Borohydrides Activated by Photogenerated Vacancies," *Journal of the American Chemical Society* 147, no. 3 (2025): 2786–2796.

12. Z. Ma, S. Panda, Q. Zhang, et al., "Improving Hydrogen Sorption Performances of MgH_2 Through Nanoconfinement in a Mesoporous CoS Nano-Boxes Scaffold," *Chemical Engineering Journal* 406 (2021): 126790.

13. L. Ren, Y. Li, Z. Li, et al., "Boosting Hydrogen Storage Performance of MgH_2 by Oxygen Vacancy-Rich H-V_2O_5 Nanosheet as an Excited H-Pump," *Nano-Micro Letters* 16, no. 1 (2024): 160.

14. G. Xia, Y. Tan, X. Chen, et al., "Monodisperse Magnesium Hydride Nanoparticles Uniformly Self-Assembled on Graphene," *Advanced Materials* 27, no. 39 (2015): 5981–5988.

15. G. Xia, Y. Tan, F. Wu, et al., "Graphene-Wrapped Reversible Reaction for Advanced Hydrogen Storage," *Nano Energy* 26 (2016): 488–495.

16. J. Zhang, W. Wang, X. Chen, J. Jin, X. Yan, and J. Huang, "Single-Atom Ni Supported on TiO_2 for Catalyzing Hydrogen Storage in MgH_2," *Journal of the American Chemical Society* 146, no. 15 (2024): 10432–10442.

17. R. Zou, J. Adedeji Bolarin, G. Lei, et al., "Microwave-Assisted Reduction of Ti Species in MgH_2-TiO_2 Composite and Its Effect on Hydrogen Storage," *Chemical Engineering Journal* 450 (2022): 138072.

18. X. Zhang, Y. F. Liu, Z. H. Ren, et al., "Pan, Realizing 6.7 Wt.% Reversible Storage of Hydrogen at Ambient Temperature With Non-Confined Ultrafine Magnesium Hydrides," *Energy & Environmental Science* 14, no. 4 (2021): 2302–2313.

19. T. T. Le, C. Pistidda, V. H. Nguyen, et al., "Nanoconfinement Effects on Hydrogen Storage Properties of MgH_2 and $LiBH_4$," *International Journal of Hydrogen Energy* 46, no. 46 (2021): 23723–23736.

20. G. Liang, J. Huot, S. Boily, A. Van Neste, and R. Schulz, "Catalytic Effect of Transition Metals on Hydrogen Sorption in Nanocrystalline Ball Milled MgH_2 –Tm (Tm-Ti, V, Mn, Fe and Ni) Systems," *Journal of Alloys and Compounds* 292, no. 1-2 (1999): 247–252.

21. L. Ren, Y. Li, N. Zhang, et al., "Nanostructuring of Mg-Based Hydrogen Storage Materials: Recent Advances for Promoting Key Applications," *Nano-Micro Letters* 15, no. 1 (2023): 93.

22. A. Schneemann, J. L. White, S. Kang, et al., "Nanostructured Metal Hydrides for Hydrogen Storage," *Chemical Reviews* 118, no. 22 (2018): 10775–10839.

23. Y. Liu, H. Du, X. Zhang, Y. Yang, M. Gao, and H. Pan, "Superior Catalytic Activity Derived From a Two-dimensional Ti_3C_2 Precursor Towards the Hydrogen Storage Reaction of Magnesium Hydride," *Chemical Communications* 52, no. 4 (2016): 705–708.

24. X. Hu, X. Chen, X. Zhang, et al., "Situ Construction of Interface With Photothermal and Mutual Catalytic Effect for Efficient Solar-Driven Reversible Hydrogen Storage of MgH_2," *Advanced Science* 11 (2024): 2400247.

25. L. Ren, W. Zhu, Y. Li, et al., "Oxygen Vacancy-Rich 2D TiO_2 Nanosheets: A Bridge Toward High Stability and Rapid Hydrogen Storage Kinetics of Nano-Confined MgH_2," *Nano-Micro Letters* 14, no. 1 (2022): 144.

26. M. Zhang, X. Xiao, X. Wang, et al., "Excellent Catalysis of TiO_2 Nanosheets With High-Surface-Energy (001) Facets on the Hydrogen Storage Properties of MgH_2," *Nanoscale* 11, no. 15 (2019): 7465–7473.

27. W. Zhu, S. Panda, C. Lu, et al., "Using a Self-Assembled Two-Dimensional MXene-Based Catalyst (2D-Ni@Ti_3C_2) to Enhance Hydrogen Storage Properties of MgH_2," *ACS Applied Materials & Interfaces* 12, no. 45 (2020): 50333–50343.

28. Y. Meng, S. Ju, W. Chen, et al., "Design of Bifunctional Nb/V Interfaces for Improving Reversible Hydrogen Storage Performance of MgH_2," *Small Structures* 3, no. 10 (2022): 220119.

29. X. Zhang, Z. Shen, N. Jian, et al., "A Novel Complex Oxide TiVO3.5 as a Highly Active Catalytic Precursor for Improving the Hydrogen Storage Properties of MgH2," *International Journal of Hydrogen Energy* 43, no. 52 (2018): 23327–23335.

30. J. Zhu, H. Wang, Y. Zhai, et al., "Cr-Doped TiO_2 Catalyzing Fast Hydrogen Absorption of MgH_2 at Subzero Temperatures," *ACS Applied Energy Materials* 7, no. 15 (2024): 6667–6676.

31. X. Zhang, X. Zhang, L. Zhang, et al., "Remarkable Low-Temperature Hydrogen Cycling Kinetics of Mg Enabled by VH_x Nanoparticles," *Journal of Materials Science & Technology* 144 (2023): 168–177.

32. Y. Qin, J. Hu, Z. Yang, et al., "Constructing VO/V_2O_3 Interface to Enhance Hydrogen Storage Performance of MgH_2," *Journal of Magnesium and Alloys* 12, no. 12 (2024): 4877–4886.

33. Z. Liu, H. Ning, R. Liu, et al., "Fabrication of V_2O_3-TiO_2-rGO Ternary Heterojunction Composite to Enhance the Hydrogen Storage Performance of MgH_2," *Chemical Engineering Journal* 499 (2024): 155877.

34. S. Ding, Y. Qiao, X. Cai, et al., "A Novel Carbon-Induced-Porosity Mechanism for Improved Cycling Stability of Magnesium Hydride," *Journal of Magnesium and Alloys* 13, no. 3 (2025): 1341–1352.

35. H. Guan, J. Liu, X. Sun, et al., "Titanium–Nickel Dual Active Sites Enabled Reversible Hydrogen Storage of Magnesium at 180°C With Exceptional Cycle Stability," *Advanced Materials* 37, no. 26 (2025): 2500178.

36. H. Wan, X. Yang, S. Zhou, et al., "Enhancing Hydrogen Storage Properties of MgH_2 Using FeCoNiCrMn High Entropy Alloy Catalysts," *Journal of Materials Science & Technology* 149 (2023): 88–98.

37. J. Zhang, H. Liu, C. Zhou, P. Sun, X. Guo, and Z. Z. Fang, "TiVNb-Based High Entropy Alloys as Catalysts for Enhanced Hydrogen Storage in Nanostructured MgH2," *Journal of Materials Chemistry A* 11, no. 9 (2023): 4789–4800.

38. X. Zhou, H. Guan, H. Lu, et al., "The Anionic Tx Defects of Nb2CTx MXene as the Effective Catalytically Active Center for the Mg-Based Hydrogen Storage Materials," *Journal of Magnesium and Alloys* 13, no. 2 (2025): 571–582.

39. X. Zhang, Y. Sun, S. Ju, et al., "Solar-Driven Reversible Hydrogen Storage," *Advanced Materials* 35, no. 2 (2023): 2206946.

40. L. Sun, Q. Li, Y. Xu, et al., "Tunable Hydrogen Coverage on Electron-Deficient Platinum Nanoparticles for Efficient Hydrogenation Reactions," *Nano Research* 16, no. 7 (2023): 8751–8756.

Supporting Information

Additional supporting information can be found online in the Supporting Information section.

Supporting Information file 1: sus270048-sup-0001-SuppMat.docx